Machine learning classification of integrin-expression-based magnetic sorted SW 620 cells by simultaneous O-PTIR and SERS

Blair L. Rist[#], Spencer A. Witte[#], Zachary D. Schultz[*]

Department of Chemistry and Biochemistry, The Ohio State University, Columbus, Ohio 43210, United States

* Corresponding author email: schultz.133@osu.edu

[#] Equal author contributions

Abstract

Immortalized cell lines are commonly used for in vitro studies such as drug efficacy, toxicology, and life-cycle due to their cost effectiveness and accessibility; however, subpopulations within a cell line can arise from random mutations or asynchronous cell cycles which may lead to results that make interpretation difficult. A method that could classify these differences and separate unique subpopulations would increase understanding of heterogeneous cellular responses. In the present work, we explore spectroscopic signals associated with subpopulations of cells magnetically sorted on the basis of $\alpha_5\beta_1$ integrin binding to cyclic-RGDfC which mimics fibronectin in the extracellular matrix. SW620 colon cancer cells were incubated with cyclic-RGDfC functionalized gold-coated, iron core nanoparticles and magnetically sorted. The subpopulations from the sort were imaged (N=10 positive and N=10 negative, number of cells) via simultaneous surface-enhanced Raman scattering (SERS) and optical-photothermal infrared spectroscopy (O-PTIR). Pearson correlations of the standard peptide-protein interaction in the SERS channel allowed for visualization of the cyclic RGDfC – integrin $\alpha_5\beta_1$ interaction. Partial least squares discriminant analysis of the O-PTIR spectra collected from cell maps successfully classified the positively or negatively sorted cells. These results demonstrate that biochemical changes within a single cell line can be sorted via an integrin activity-based assay using simultaneous SERS and O-PTIR.

Colorectal cancer is a common malignant cancer that is currently the third leading cause of cancer death in the world resulting from the accumulation of genetic and epigenetic mutations whose most common treatment is surgery.[1,2] Still, about 50% of colorectal cancer patients experience recurrence and metastasis of their tumor. The SW620 cell line is an immortalized cell line derived from the metastatic site in the large intestine. This cell line has been well studied including works on this cell lines' common gene mutations in comparison to multiple other cell lines,[3] as well as it's expression of various integrin domains.[4,5] While immortalized cell lines are often used for extensive studies, it has also been reported that tumor heterogeneity can be seen in a single cell line after passaging either through mutations or the idea of "stemness" that can lead to cellular subpopulations.[6,7] A method that can easily separate and then identify different cellular subpopulations would then increase understanding of cell heterogeneity and implications for disease.

The current methods used to measure the phenotypic differences of heterogenous tumors include immunofluorescence, mass spectrometry, and RNA sequencing. Immunofluorescence targets specific phenotypic features, commonly proteins, of the cells with fluorescent markers to visualize differences;[8] however, the structure of the general sites of antibody affinity have led them to be multispecific which can lead to difficulty in quantifying more heterogeneous tumours.[9,10] Immunofluorescence is typically restricted to 4 or 5 markers maximum,[8] limiting options for subpopulation classification. Other works have utilized mass spectrometry to analyze peptide content within cells.[11] Mass spectrometry approaches are inherently destructive, require extensive sample preparation, and may not reveal protein activity. As a nontargeted and multiplexed measurement, mass spectrometry require extensive separation and bioinformatics that have limited research.[12,13] The current gold standard is single cell RNA-sequencing which has been shown to be quite successful in identifying cellular subpopulations[14] and cell cycle differences.[15] Isolating a single cell from an organ and tissue is challenging and procedures have low throughput.[16–18] Additionally, single cell studies usually only contain about 10 picograms of RNA on averages and even less mRNA.[19,20] RNA sequencing requires an amplification step to accurately measure but not all cRNA is amplified linearly, leading to disproportional representation of the cDNA in a cell.[19]

Magnetically activated cellular sorting (MACS) is a separation technique that utilizes magnetic particles bound to cells to sort heterogeneous populations of cells into different subpopulations. Traditionally MACS is performed using antibodies that target surface antigens on the cells. There have been many studies that focus on sorting cancer stem cells with antibodies such as CD24, CD44, CD144[21–23] or with other antibodies targeting other antigens on the cell surface.[24,25] Antibody based sorting increases in utility as fabrication techniques continue to improve affinity. [26,27] Targeting receptor activity provides some advantages over antibodies. Integrin proteins are one of the most studied and prevalent surface receptors, and are known to have different conformational forms that contribute to their binding affinity.[28–32] Cellular pathways can be activated through the binding of integrin proteins, consisting of α and β domains that specify which ECM components they recognize for binding.[33–35] These extracellular matrix components can be mimicked with small peptides such as the—particularly well known interaction—Arg-Gly-Asp (RGD) peptide mimic known to bind to integrins $\alpha_5\beta_1$ and $\alpha_v\beta_3$.[36–38]

Previously, RGDfC functionalized plasmonic nanoparticles were incubated with SW620 cells. These cells were imaged by surface enhanced Raman scattering (SERS), allowing for specific peptide-integrin interactions to be differentiated.[39] Initial studies have shown that subpopulations of SW620 and SW480 cells can be magnetically sorted using the Cyclic RGDfC and CDPGYIGSR peptides, extracellular matrix mimics for fibronectin and laminin, functionalized onto gold coated magnetic nanoparticles.[40] With these probes, SERS has shown that the peptides specifically bind to their corresponding integrins and that cells separated by the magnetic system show a SERS signal that corresponds to the expected integrin interactions while the cells that were separated show no particle binding. However, besides the presence of bound particles and their integrin signal, little could be said about the biological differences of the rest of the cellular components that gave rise to these subpopulations.

Infrared (IR) and Raman spectroscopy are complementary vibrational spectroscopic techniques that can provide information on the biological structure and chemical changes within cells. Typical single-cell analyses by IR spectroscopy suffer from low spatial resolution due to the diffraction limit of mid-IR radiation. Furthermore, strong absorption due to water and Mie scattering artifacts can limit the use of IR signals from biological samples.[41] On the contrary, Raman is insensitive to water, but Raman scattering events have a low probability which can be further obscured by the background fluorescence that is typical in biological samples. Raman signals can be enhanced by incorporating plasmonic nanostructures into the sample mainly due to the enhanced local electric field caused by the localized surface plasmon resonance, thereby enhancing the scattered field; i.e., SERS.[42]

Optical-photothermal infrared spectroscopy (O-PTIR) is an emerging alternative to traditional IR spectroscopy where the broadband source is replaced with a Quantum Cascade Laser (QCL). O-PTIR combines a pulsed QCL source of mid-IR radiation with a visible or near-IR probe beam for optical detection to enable higher spatial resolution imaging.[43,44] O-PTIR leverages the change in refractive index due to heating by a selective absorption at specific infrared frequencies from a pulsed infrared laser. The pulsed heating encodes an optical distortion in the visible pump beam incident within the infrared laser spot. The visible probe beam decouples the spatial resolution of the IR absorption from the wavelength of the infrared source, which leads to improved, IR-frequency-independent spatial resolution and also avoids Mie scattering artifacts.[41] Moreover, Raman scattered light from the probe beam incident on the sample can be collected—simultaneously—yielding both high quality IR and Raman vibrational information from the same sample spot. Herein, the highly specific peptide-protein binding information afforded by SERS of integrin-bound peptide-functionalized nanoparticles is combined with high quality O-PTIR absorbance spectra of the rest of the cell to differentiate and explain biochemical differences within subpopulations of the SW620 cell line.

In this paper, cyclic-RGDfC functionalized plasmonic magnetic nanoparticles are utilized to sort SW620 cells based on their integrin expression. Simultaneous imaging of both SERS and O-PTIR for both the sorted (positive) and unsorted (negative) cellular subpopulations is demonstrated. Pearson correlation coefficients between the observed and known SERS signal from peptide-protein interaction and a partial least squares discriminant analysis (PLS-DA) machine learning approach in the O-PTIR channel allowed the subpopulations to be classified based on biomolecular fingerprints. These results demonstrate clear biomolecular differences among cells sorted by their integrin-activity.

Experimental Section

Additional details of procedures are included in the supporting information.

Chemicals and Materials

Absolute Mag gold coated magnetic nanoparticles (capped with citrate, 250 nm diameter) were purchased from CD Bioparticles. Cyclic Arg – Gly - Asp -D – Phe – Cys (RGDfC), ≥95% was purchased from Biosynth. Human Integrin $\alpha_5\beta_1$, CF ≥90% was purchased from R&D systems. Ultrapure water (18.2 MΩ cm) from a Thermo Scientific GenPure UB-TOC/UF xCAD water purification system was used. Phosphate buffered saline with Calcium and Magnesium (DPBS) was bought from Gibco Life Technologies Corporation. RPMI Medium was purchased from ThermoFischer Scientific. Fetal Bovine Serum one shots were purchased from Gibco. The SW 620 cell line was purchased from American Type Cell Culture (ATCC, Manassas, VA, USA). EasySep sorting buffer and magnetic separation system were purchased from Stem Cell Technologies. All chemicals were used without further purification. Aluminum coated glass slides were purchased from Platypus Technologies and Calcium Fluoride Windows (Ø1/2" CaF2 Broadband Precision Window, Antireflective Coated: 1.65 - 3.0 µm) were purchased from Thorlabs.

Methods

Nanoparticle functionalization, cellular recovery and cellular sorting followed the procedure previously reported in earlier studies.[40] Additional details regarding the methods can be found in the supporting information and **Figure S1**.

Simultaneous IR and Raman of Positive and Negative Cells

Simultaneous O-PTIR and Raman spectroscopy were performed on a mIRage-LS (Photothermal Spectroscopy Corp., Santa Barbara, CA) equipped with a 785 nm probe beam on both the positive (N=10) and negative (N=10) sorted cells. The pulsed QCL was co-located with the probe beam through a 40X Cassegrain objective. The QCL was scanned at the sample, and IR absorbances were detected by modulations of the 785 nm probe beam due to changes in the sample's optical properties via heating. The intensity changes were detected and demodulated by a lock-in amplifier at the repetition rate of the QCL. Hyperspectral data cubes were acquired in both the O-PTIR and Raman channel in lateral 1x1 µm steps. O-PTIR data were acquired at 200 cm^{-1}/s over three co-averages and excited with 47% QCL power and 9% probe power. The standard photodiode was utilized at 2x gain. Raman data were acquired through a 75 µm pinhole for 2 s integrations averaged 11 times and dispersed with a 600 lines/mm grating.

Spectral analysis and machine learning

Detailed descriptions of spectral analysis for both the SERS and O-PTIR images can be found in the supporting information under **Spectral data treatment**.

Results and Discussion

Integrin binding

Magnetic gold coated nanoparticles were functionalized with the cyclic RGDfC peptide, meant to mimic fibronectin in the extracellular matrix which integrin $\alpha_5\beta_1$ targets[37,40]. The particles were then incubated with integrin $\alpha_5\beta_1$ for 2 hours in DPBS with calcium and magnesium. After incubation, 10 µL of this suspension was then dropped onto an aluminum covered glass slide and allowed to dry under an external magnetic field. In-situ Raman spectra were collected using 9% power with a 75 µm pinhole and 40X Cassegrain objective over areas of aggregated particles. Spectra with signal above the integrated threshold (**Figure S2**) were imported into Matlab and analyzed by multivariate curve resolution-alternating least squares (MCR-ALS). **Figure S3A** shows the generated MCR components from the in-situ peptide-functionalized particles and protein interaction. Component 1 is assigned to nonspecific interactions or molecules nearby the particles, and component 2 is assigned to the peptide-protein interaction. This assignment was made due to the presence of the 1012 cm^{-1} feature characteristic of phenylalanine[45] in the peptide which has been previously reported for this particular peptide-protein interaction, as well as the 296 cm^{-1} stretch indicative of the Fe_2O_3 core of the magnetic nanoparticles.[46] Other important features include the 672 cm^{-1} peak due to the presence of tryptophan in the integrin protein as well as the presence of tyrosine indicated by the 872 and 1606 cm^{-1} peaks.[47,48] **Figure S3B** shows component 2 in comparison to the average SERS spectrum from the cyclic RGDfC – Integrin $\alpha_5\beta_1$ interaction. Whilst the signal originating from buffers, salts and substrate still has a strong presence in the averaged spectrum, the indicative phenylalanine stretch at 1012 cm^{-1} is still quite prevalent.

Simultaneous detection of IR and Raman for negative and positively sorted cells

To characterize the chemical signals from cells sorted based on their binding to the RGDfC-functionalized plasmonic magnetic particles, the particles were incubated with the SW620 cells, sorted magnetically, fixed with paraformaldehyde, and hyperspectral O-PTIR and Raman maps were obtained. Pearson correlation maps were generated for each cell comparing the spectrum to MCR component 2 indicative of the peptide- protein interaction (**Figure S3A**). The results of the Pearson correlation analysis of one positive cell as described above is reflected in **Figure 1A**. It is observed that the peptide-protein interaction is localized heavily within the cell, whereas the O-PTIR cell map plotted as the integrated spectral area under curve (AUC) of the same positive cell (**Figure 1B**) and an example negative cell (**Figure 1C**) show variations in spectral intensity without distinction between the positive or negative cell. The region of the SERS map in **Figure 1A** with the highest correlation to the standard peptide protein interaction is plotted in **Figure 1D** and shows the characteristics of the peptide protein interaction over top of the background from the CaF_2 substrate used here. Additionally, O-PTIR spectra (**Figure 1E, F**) pulled out from the cell maps show the differences in O-PTIR intensity at pixels on the cell with large response (green traces), moderate responses (blue trace), and completely off the cell (purple trace).

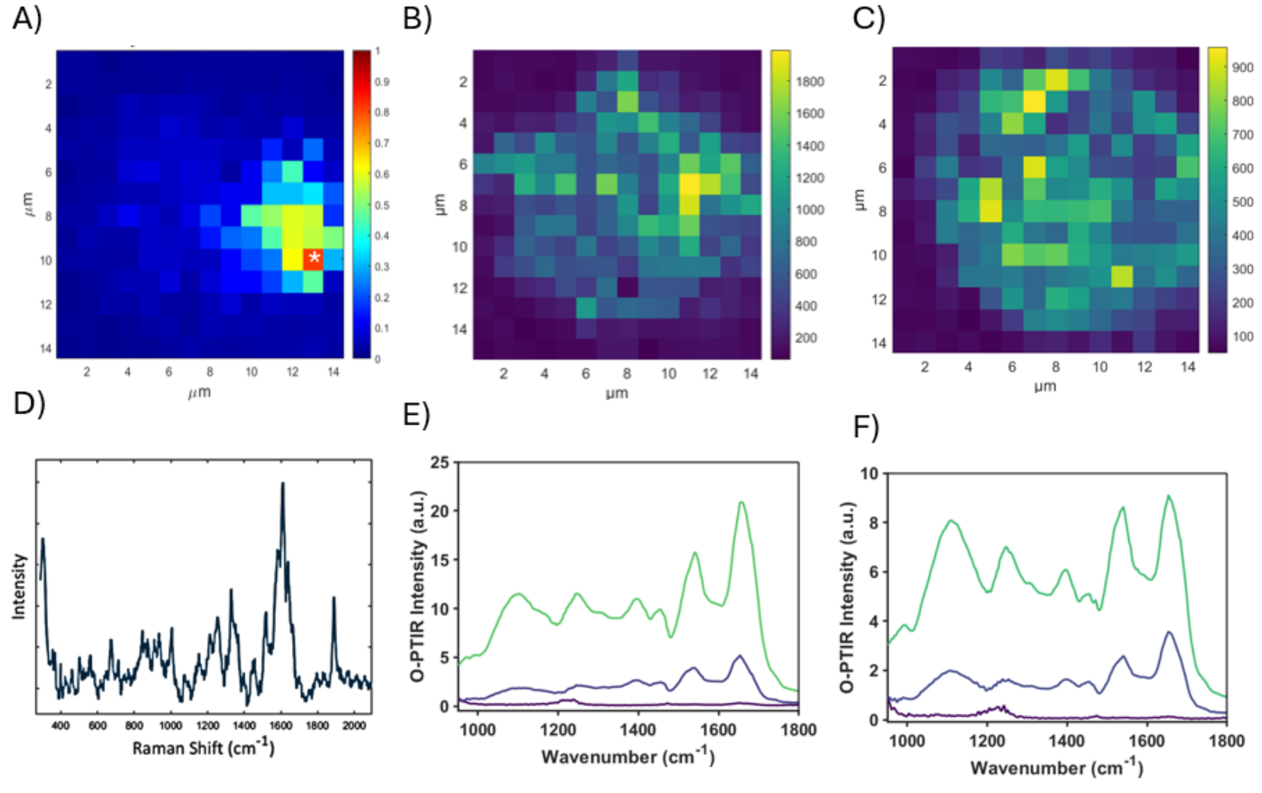

Figure 1.A) Pearson correlation SERS map of RGDfC- Integrin $\alpha_5\beta_1$ interaction on positive cell 5 with asterisk denoting spectrum that is plotted. The O-PTIR integrated spectral AUC images from the positive cell 5 (B) and a negative cell (C), respectively. D) spectrum pulled out from SERS Pearson correlation map as denoted by asterisk. E,F) O-PTIR spectra from positive (E) and negative (F) O-PTIR cell maps, respectively. The colors of the spectra correspond to the pixel intensity in the corresponding cell map.

The white light images of three positively (**Figure 2A**) and negatively sorted cells (**Figure 2B**) are compared to the integrated intensity maps from each cell as well as the integrated intensity maps masked based on particle presence indicated by detecting a Raman iron oxide band at 296 cm^{-1}. The cell maps for all 10 cells for each subpopulation are shown in **Figure S4-S5**. Both the positive and negative cell subpopulations exhibit similar integrated IR intensities in the obtained maps that reflect the morphology of the cells studied (**Figure 2, S4, S5**). The acquired SERS maps elucidate the presence of integrin bound nanoparticles in the positive sort which can be differentiated from the lack of response in the unsorted negative subpopulation (**Figure 2, S4, S5**). These images establish that there is no correlation between the O-PTIR intensities and the presence of a plasmonic nanoparticle, suggesting that surface enhanced infrared absorption spectroscopy (SEIRAS) does not contribute to the infrared signals. It is worth noting that only 30% of the positive cells imaged in this paper demonstrated high correlation in the Pearson correlation maps (**Figure 2A**), but 90% of the positive cells showed at least one spectrum with an iron-oxide response (**Figure S4**). There are isolated spectra in the negative sorted subpopulation that also show an iron-oxide spectral response (**Figure S5**).

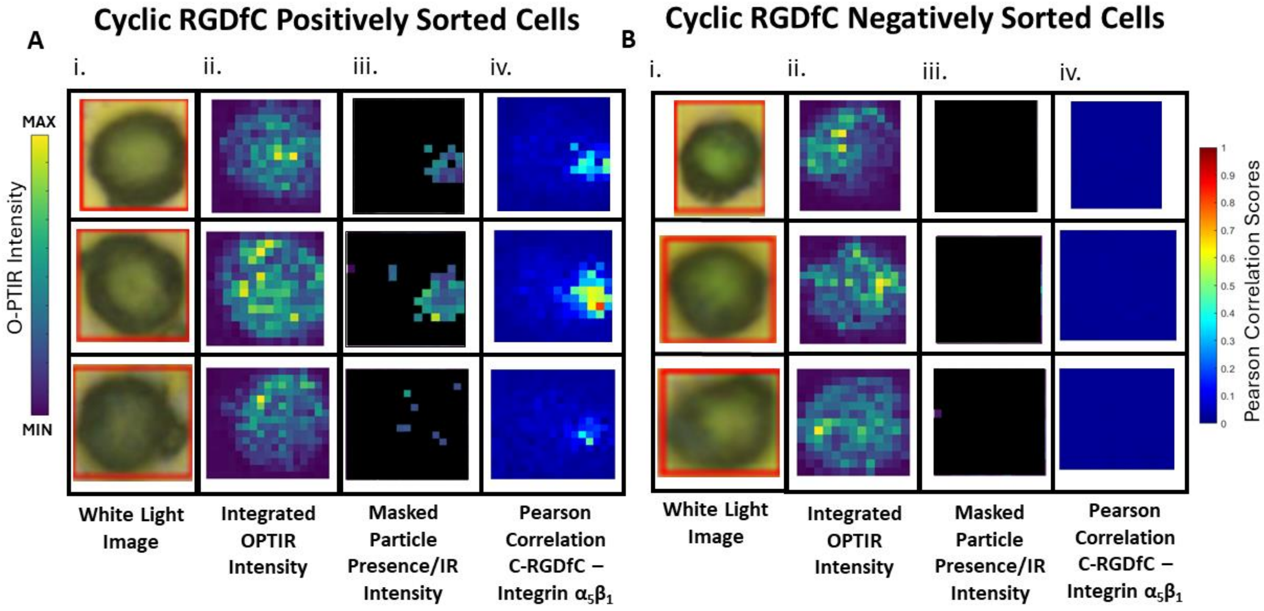

Figure 2. Representative white light and spectral SW 620 cell images from simultaneous O-PTIR and SERS array imaging for (A) positively sorted cells and (B) negatively sorted cells. White light images for the positive and negative sort are given in column i. After baseline correction, the total integrated O-PTIR spectral intensity is plotted over the dimensions of the hyperspectral image in column ii. Using the Raman spectral signature of the iron-oxide stretch (296 cm^{-1}), the location of particles is visualized in iii, and it is plotted over the integrated O-PTIR intensity at each pixel of the mapped area. In column iv, the Pearson correlation scores of the Raman spectral map to the MCR model of the integrin-cyclic RGDfC interaction model are plotted over the imaged dimensions. Each row is a biological replicate from the same positively sorted (A) or negatively sorted (B) cell.

PLS-DA model classification of negatively and positively sorted cells

While the integrated IR intensities in the O-PTIR maps do not show significant differences between the positive and negative subpopulations, analysis of the spectra in each map provides information about the rest of the cell that could be used to classify the subpopulations. Further pre-processing of the O-PTIR spectra was required to remove the off-cell spectra (e.g., **Figure 1E, F**) and low S/N spectra. After removal by setting a statistical threshold of the integrated area for all spectral observations for each cell (**Figure S6**), the 2nd derivative spectrum for each observation was calculated as described in the supporting information (see **O-PTIR data preprocessing**). Principal component analysis (**Figure S7-S8**) does not show clear separation between the positive and negatively sorted subpopulations. The 2nd derivative spectral data and their respective class labels were mean-centered, and four-latent variables (LV) PLS-DA model was constructed, and random subsets cross-validation (CV) was performed. The optimized model summary CV statistics are given in **Table 1**. In **Figure 3**, the receiver operating characteristic (ROC) curve analysis is shown for each subpopulation. The ROC curves (**Figure 3**) have high AUC with nearly perfect overlap between the calibration and CV curves for both the positively and negatively sorted cells. After four LVs (**Figure S9A**) the calibration and CV RMS error have a larger difference, implying a higher risk of overfitting the model. The variable importance in projection (VIP scores) in **Figure S9B** indicate the vibrational modes important for this classification model are centered at, 967, 1045, 1077, 1139, 1187, 1239, 1419, 1441, 1543, 1653, and 1737 cm^{-1}.

Table 1. Summary statistics of random subsets cross-validation for PLS-DA 4 LV model.

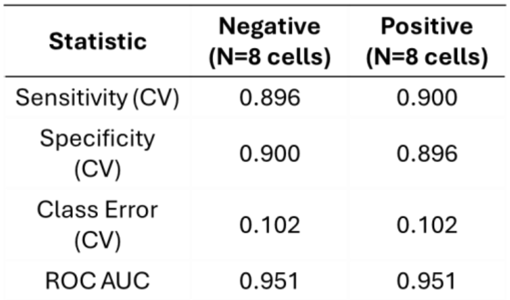

Statistic	Negative (N=8 cells)	Positive (N=8 cells)
Sensitivity (CV)	0.896	0.900
Specificity (CV)	0.900	0.896
Class Error (CV)	0.102	0.102
ROC AUC	0.951	0.951

The PLS-DA model was built from the positive spectral stack and excluded spectra correlated to the particle presence as shown in **Figure S10**. It can be seen in **Figure S11** that the VIP scores for the model built without the particle-correlated spectra and the model summarized in **Table 1** are nearly identical. Additionally, the performance of the model without the particle correlated spectra (**Table S1**) is close to the optimized model with the particle-correlated spectra included (**Table 1**). This indicates that the classification derives from biomolecular differences between the sorted and unsorted cells and is not a result of spectral modulations due to the plasmonic magnetic nanoparticles. It is worth noting that the scores for both models show a high degree of similarity (**Figure S12**) as well as the LVs (**Figure S13**). Conclusions about which vibrational signatures are important in classifying these cellular subtypes can be made independent of the model analyzed since their performance and construction are equivalent.

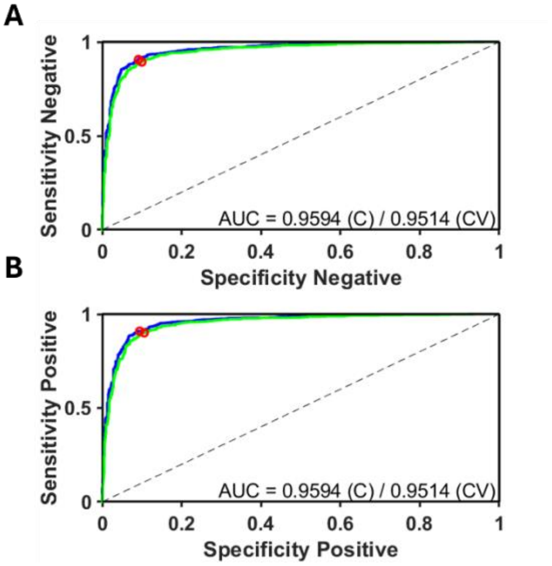

Figure 3. PLS-DA model construction and optimization performed on the data filtered by spectral AUC. A,B) Receiver operating characteristic curves (ROC) for the negative unsorted cells (A) and positive sorted cells (B).Calibration data is shown in the blue traces and random sets cross-validation is shown in the green traces.

Analysis of the VIP scores for both models (**Figure S11**) and comparison of those important variables with the overlaid 2nd derivative spectra (**Figure 4**) suggest biochemical differences based on the functional groups driving the PLS-DA sort. The most significant change is in the amide I region between 1620-1690 cm^{-1} which is related to ν(C=O) in protein backbone.[49] There are relative intensity changes between the subpopulations for the bands centered at 1653 and 1639 cm^{-1}, and the negative population has a lower overall intensity on the higher wavenumber side of the band (>1650 cm^{-1}) (**Figure 4**). It has been shown that the relative intensity of the amide I band is related to protein secondary structure,[50] which implies differences in the structure of the near-surface proteins on the SW620s herein. Moreover, these structural differences likely originate from near the cell surface as the penetration of the mid-IR source would be attenuated deeper into the cell. The shift in protein structure in the average spectra agrees with the idea that integrins have different conformations related to their activity—whether ECM components (or peptide mimics) bind or not.

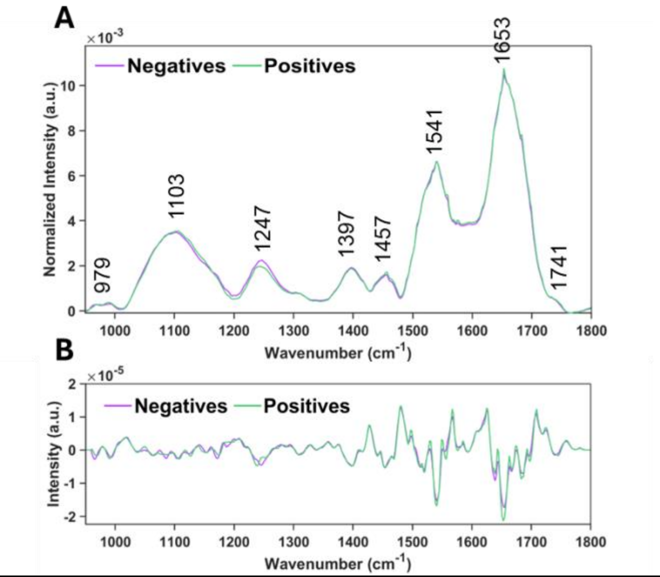

Figure 4. A) The average spectrum for negative cells (purple) and positive (green) cells after removing low S/N spectra from image are overlaid. Peaks identified in the VIP scores are labeled. B) The second derivative of the spectra are shown to highlight spectral differences.

Changes are observed in the positive and negative cell subpopulations between 1000-1300 cm^{-1} that indicate differences in the DNA/RNA content and carbohydrate residues.[51,52] In **Figure 4B**, the signals from 1030-1180 cm^{-1} show relative intensity changes as evidenced by the lack of overlap between the purple (negatives) and green (positives) traces. These differences reflect changes in the $\nu_s(PO_2^-)$ band (~1081 cm^{-1}) and ν_{as}(CO-O-C) (~1165 cm^{-1}) which are related to nucleic acids, polysaccharides, and ribose ring formations. There is a frequency shift and intensity difference at ~1241 cm^{-1} in the $\nu_{as}(PO_2^-)$ band due to phosphodiester linkages in DNA.[51–54] The band at 1399 cm^{-1} is due to $\nu_s(COO^-)$ related to fatty acids of which the shoulder around 1419 cm^{-1} shows significance in the VIP scores (**Figure S11**) .[55] The frequency shift from 1239 (positives) to 1245 (negatives) cm^{-1} of the asymmetric phosphodiester stretching mode implies a shift from higher DNA content to higher RNA content, respectively.[56–59] This disparity in the nucleic acid content is consistent with cell cycle changes and agrees with the large differences in the protein structure that the model is keying on (**Figure S11**), as the cell surface receptors are expected to change activity during the cell cycle. More evidence for DNA/RNA changes comes from the ribose-phosphate skeletal motions band at around 970 cm^{-1}.[59,60] In the positive sort, increased DNA content implies that the cells have synthesized more DNA, a phenomena usually expected prior to mitosis in the S or G2 phase of the cell cycle. These observations and their correspondence to the PLS-DA model are summarized in **Table S2**.

To validate the model, the spectra from held out O-PTIR cell maps were scored with particle-correlated spectra left in. The validation samples consisted of spectra from cells 9 and 10 from the positive and negative subpopulations (**Figure S4-S5**). The probabilities of class membership for all the spectra in the cell maps are shown in **Figure 5**. Most of the spectra for the two held out cells have greater than a 50% probability of belonging to their correct class. These validation results are summarized in **Table S3**. It is worth noting that in the positive validation cells that only cell 9 (**Figure S4**) shows indications of nanoparticles present based on the SERS Pearson correlation. This further confirms the O-PTIR based classification does not arise from nanoparticle effects on the IR spectra in the PLS-DA model but rather intrinsic biochemical differences in the sorted cells. Model validation statistics show greater than 80% classification accuracy (**Table S3**), implying that the cell subtypes are correctly classified when scoring spectral data on the PLS-DA model.

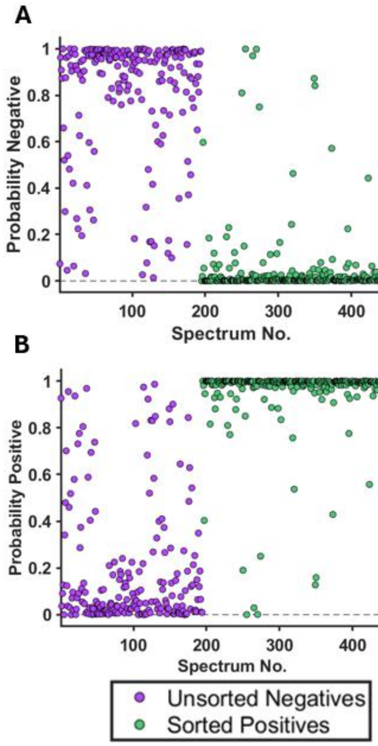

Figure 5. The probability a spectrum from held out positive and negative sorted cells being classified as by the model as belonging to A) the negative cell subpopulation, and B) the positive sorted cell subpopulation is shown. The correct classification on distinct validation samples supports the biochemical changes underlying the classification.

This method has the potential to classify subclasses of cancerous cells based on biochemical differences that may influence prognosis and targeted therapy. Integrins are tied to cellular pathways that help differentiate cells. Fibronectin, which is mimicked here by the c-RGDfC, interacts with the integrin $\alpha_5\beta_1$ receptor. This interaction is believed to help cellular proliferation and is tied to progression of the cell line from the G_1 to S phase of the cell cycle.[61–64] As reported above, there appears to be higher DNA concentration within the positive cells which is consistent with progression from the G_1 to S phase of the cell cycle; producing more DNA in the process. RNA content is also reported to increase from the G1 phase through the S phase, being the lowest during the mitotic phase; however, DNA synthesis is the primary event in the S phase.[65] This increase in nucleic acid concentration within the S phase present in IR data has been shown before.[66] However, previous IR measurements of the cell cycle have also seen low presence of the nucleic acid bands in the other phases (negatively sorted population) while the response observed here shows subtler changes in nucleic acid content.[66,67] This may be explained because typical IR microscopy (e.g., FTIR) has an image resolution around ~10 μm--approximately the size of a cell. This poorer spatial resolution might average out compact DNA regions that would be present in the G_1 or G_2 phase relative to the wider distribution of DNA in the S phase. The increased spatial resolution of O-PTIR enables higher signal-to-background for smaller sized cellular features, which may be facilitating classification in the present work.

Approximately 13% of the total cells were positively sorted in this study, which agrees with the previous work using these particles.[40] At any time, a majority of naturally proliferating SW620 cells are found in the M/G_1 phase.[68,69] However, importantly the G_1 phase generally lasts around 10-11 hours while the S phase can last up to 8 hours. The lower-than-expected percentage suggests that binding to the peptide may select a unique subpopulation of cells that preferentially interact with fibronectin and thus proceed into the S phase relative to all cells in the G_1 phase. This subpopulation is thus characterized by the activity of the integrin receptor.

While this study focuses on the spectral and phenotypic differences within a singular cell line and utilizes a singular ECM matrix mimic, the cancer microenvironment is more diverse than just fibronectin as mimicked here. Tumors consist of highly heterogeneous populations of malignant cells with their own heterogeneity tied to the microenvironment. This heterogeneity is what often proves difficult during treatment. Future development of probes that mimic different ECM matrix components is a potential avenue for further exploration while maintaining quick identification via OPTIR and SERS that can be paired with drug studies to help determine effective treatments.

Conclusion

Simultaneous O-PTIR and SERS performed on the subpopulations of SW620 cancer cells positively and negatively sorted based on binding to a c-RGDfC peptide functionalize magnetic bead show spectroscopic differences attributable to biochemical differences. The SERS data identifies binding of a peptide to specific receptors. Analysis of the infrared spectra in hyperspectral maps using a PLS-DA classification model further elucidates these biochemical differences between positive and negative cells. The classification model exhibits 90% classification accuracy based on cross-validation with the calibration data and a similar 90% classification accuracy in the held out positive and negative validation samples. The main discriminatory LVs projected by the model agree with the average spectral differences, and these differences are consistent with cell processes dependent on integrin-activity, primarily progression of the cell cycle from the G_1 phase to S phase of the cell cycle. This suggests that the peptide-based probes can sort for activity of the receptors in each cell and that simultaneous IR and SERS can elucidate these differences making this technique a promising technology to elucidate the differences in cell populations from more heterogeneous tumors or as a helpful tool in differentiating cellular processes.

Associated Content

The Supporting Information is available free of charge on the ACS Publications website.

Supporting information includes detailed methods, additional replicate images of cells, as well as validation models for PLS-DA discrimination.

Author Contributions

Spencer Witte and Blair Rist contributed equally to the manuscript.

Acknowledgements

This work was supported by the Ohio State University and the National Institutes of Health award R01 GM109988 and through the Comprehensive Cancer Center award P30 CA016058. The mIRage-LS microscope was acquired with support from award CHE-2117225 from the National Science Foundation. We acknowledge the center for chemical and biophysical dynamics at Ohio State for use of the mIRage-LS.

References:

(1) Rawla, P.; Sunkara, T.; Barsouk, A. Epidemiology of Colorectal Cancer: Incidence, Mortality, Survival, and Risk Factors. *Prz Gastroenterol* **2019**, *14* (2), 89–103. https://doi.org/10.5114/pg.2018.81072.

(2) Ewing, I.; Hurley, J. J.; Josephides, E.; Millar, A. The Molecular Genetics of Colorectal Cancer. *Frontline Gastroenterol* **2014**, *5* (1), 26–30. https://doi.org/10.1136/flgastro-2013-100329.

(3) Ahmed, D.; Eide, P. W.; Eilertsen, I. A.; Danielsen, S. A.; Eknæs, M.; Hektoen, M.; Lind, G. E.; Lothe, R. A. Epigenetic and Genetic Features of 24 Colon Cancer Cell Lines. *Oncogenesis* **2013**, *2* (9), e71–e71. https://doi.org/10.1038/oncsis.2013.35.

(4) Koretz, K.; Brüderlein, S.; Henne, C.; Fietz, T.; Laqué, M.; Möller, P. Comparative Evaluation of Integrin α- and β-Chain Expression in Colorectal Carcinoma Cell Lines and in Their Tumours of Origin. *Vichows Archiv A Pathol Anat* **1994**, *425* (3), 229–236. https://doi.org/10.1007/BF00196144.

(5) Schlaeppi, M.; Rüegg, C.; Trân-Thang, C.; Chapuis, G.; Tevaearai, H.; Lahm, H.; Sordat, B. Role of Integrins and Evidence for Two Distinct Mechanisms Mediating Human Colorectal Carcinoma Cell Interaction with Peritoneal Mesothelial Cells and Extracellular Matrix. *Cell Adhes Commun* **1997**, *4* (6), 439–455. https://doi.org/10.3109/15419069709004460.

(6) Marusyk, A.; Polyak, K. Tumor Heterogeneity: Causes and Consequences. *Biochimica et Biophysica Acta (BBA) - Reviews on Cancer* **2010**, *1805* (1), 105–117. https://doi.org/10.1016/j.bbcan.2009.11.002.

(7) Stockholm, D.; Benchaouir, R.; Picot, J.; Rameau, P.; Neildez, T. M. A.; Landini, G.; Laplace-Builhé, C.; Paldi, A. The Origin of Phenotypic Heterogeneity in a Clonal Cell Population In Vitro. *PLOS ONE* **2007**, *2* (4), e394. https://doi.org/10.1371/journal.pone.0000394.

(8) Loo, L.-H.; Lin, H.-J.; Steininger, R. J.; Wang, Y.; Wu, L. F.; Altschuler, S. J. An Approach for Extensibly Profiling the Molecular States of Cellular Subpopulations. *Nat Methods* **2009**, *6* (10), 759–765. https://doi.org/10.1038/nmeth.1375.

(9) Richards, F. F.; Konigsberg, W. H.; Rosenstein, R. W.; Varga, J. M. On the Specificity of Antibodies. *Science* **1975**, *187* (4172), 130–137. https://doi.org/10.1126/science.46122.

(10) Mian, I. S.; Bradwell, A. R.; Olson, A. J. Structure, Function and Properties of Antibody Binding Sites. *Journal of Molecular Biology* **1991**, *217* (1), 133–151. https://doi.org/10.1016/0022-2836(91)90617-F.

(11) Ong, T.-H.; Kissick, D. J.; Jansson, E. T.; Comi, T. J.; Romanova, E. V.; Rubakhin, S. S.; Sweedler, J. V. Classification of Large Cellular Populations and Discovery of Rare Cells Using Single Cell Matrix-Assisted Laser Desorption/Ionization Time-of-Flight Mass Spectrometry. *Anal. Chem.* **2015**, *87* (14), 7036–7042. https://doi.org/10.1021/acs.analchem.5b01557.

(12) Nemes, P.; Knolhoff, A. M.; Rubakhin, S. S.; Sweedler, J. V. Metabolic Differentiation of Neuronal Phenotypes by Single-Cell Capillary Electrophoresis–Electrospray Ionization-Mass Spectrometry. *Anal. Chem.* **2011**, *83* (17), 6810–6817. https://doi.org/10.1021/ac2015855.

(13) Rubakhin, S. S.; Churchill, J. D.; Greenough, W. T.; Sweedler, J. V. Profiling Signaling Peptides in Single Mammalian Cells Using Mass Spectrometry. *Anal. Chem.* **2006**, *78* (20), 7267–7272. https://doi.org/10.1021/ac0607010.

(14) Bartoschek, M.; Oskolkov, N.; Bocci, M.; Lövrot, J.; Larsson, C.; Sommarin, M.; Madsen, C. D.; Lindgren, D.; Pekar, G.; Karlsson, G.; Ringnér, M.; Bergh, J.; Björklund, Å.; Pietras, K. Spatially and Functionally Distinct Subclasses of Breast Cancer-Associated Fibroblasts Revealed by Single Cell RNA Sequencing. *Nat Commun* **2018**, *9* (1), 5150. https://doi.org/10.1038/s41467-018-07582-3.

(15) Riba, A.; Oravecz, A.; Durik, M.; Jiménez, S.; Alunni, V.; Cerciat, M.; Jung, M.; Keime, C.; Keyes, W. M.; Molina, N. Cell Cycle Gene Regulation Dynamics Revealed by RNA Velocity and Deep-Learning. *Nat Commun* **2022**, *13* (1), 2865. https://doi.org/10.1038/s41467-022-30545-8.

(16) Tang, F.; Barbacioru, C.; Wang, Y.; Nordman, E.; Lee, C.; Xu, N.; Wang, X.; Bodeau, J.; Tuch, B. B.; Siddiqui, A.; Lao, K.; Surani, M. A. MRNA-Seq Whole-Transcriptome Analysis of a Single Cell. *Nat Methods* **2009**, *6* (5), 377–382. https://doi.org/10.1038/nmeth.1315.

(17) Xue, Z.; Huang, K.; Cai, C.; Cai, L.; Jiang, C.; Feng, Y.; Liu, Z.; Zeng, Q.; Cheng, L.; Sun, Y. E.; Liu, J.; Horvath, S.; Fan, G. Genetic Programs in Human and Mouse Early Embryos Revealed by Single-Cell RNA Sequencing. *Nature* **2013**, *500* (7464), 593–597. https://doi.org/10.1038/nature12364.

(18) Kamme, F.; Salunga, R.; Yu, J.; Tran, D.-T.; Zhu, J.; Luo, L.; Bittner, A.; Guo, H.-Q.; Miller, N.; Wan, J.; Erlander, M. Single-Cell Microarray Analysis in Hippocampus CA1: Demonstration and Validation of Cellular Heterogeneity. *J. Neurosci.* **2003**, *23* (9), 3607–3615. https://doi.org/10.1523/JNEUROSCI.23-09-03607.2003.

(19) Potter, S. S. Single-Cell RNA Sequencing for the Study of Development, Physiology and Disease. *Nat Rev Nephrol* **2018**, *14* (8), 479–492. https://doi.org/10.1038/s41581-018-0021-7.

(20) Wang, Y.; Navin, N. E. Advances and Applications of Single-Cell Sequencing Technologies. *Molecular Cell* **2015**, *58* (4), 598–609. https://doi.org/10.1016/j.molcel.2015.05.005.

(21) Zhu, Z.; Hao, X.; Yan, M.; Yao, M.; Ge, C.; Gu, J.; Li, J. Cancer Stem/Progenitor Cells Are Highly Enriched in CD133+CD44+ Population in Hepatocellular Carcinoma. *International Journal of Cancer* **2010**, *126* (9), 2067–2078. https://doi.org/10.1002/ijc.24868.

(22) Sahlberg, S. H.; Spiegelberg, D.; Glimelius, B.; Stenerlöw, B.; Nestor, M. Evaluation of Cancer Stem Cell Markers CD133, CD44, CD24: Association with AKT Isoforms and Radiation Resistance in Colon Cancer Cells. *PLOS ONE* **2014**, *9* (4), e94621. https://doi.org/10.1371/journal.pone.0094621.

(23) Baumann, M.; Krause, M.; Thames, H.; Trott, K.; Zips, D. Cancer Stem Cells and Radiotherapy. *International Journal of Radiation Biology* **2009**, *85* (5), 391–402. https://doi.org/10.1080/09553000902836404.

(24) Schmitz, B.; Radbruch, A.; Kümmel, T.; Wickenhauser, C.; Korb, H.; Hansmann, M. l.; Thiele, J.; Fischer, R. Magnetic Activated Cell Sorting (MACS) — a New Immunomagnetic Method for Megakaryocytic Cell Isolation: Comparison of Different Separation Techniques. *European Journal of Haematology* **1994**, *52* (5), 267–275. https://doi.org/10.1111/j.1600-0609.1994.tb00095.x.

(25) Jia, Z.; Liang, Y.; Xu, X.; Li, X.; Liu, Q.; Ou, Y.; Duan, L.; Zhu, W.; Lu, W.; Xiong, J.; Wang, D. Isolation and Characterization of Human Mesenchymal Stem Cells Derived from Synovial Fluid by Magnetic-Activated Cell Sorting (MACS). *Cell Biology International* **2018**, *42* (3), 262–271. https://doi.org/10.1002/cbin.10903.

(26) Tajima, N.; Takai, M.; Ishihara, K. Significance of Antibody Orientation Unraveled: Well-Oriented Antibodies Recorded High Binding Affinity. *Anal. Chem.* **2011**, *83* (6), 1969–1976. https://doi.org/10.1021/ac1026786.

(27) Bostrom, J.; Lee, C. V.; Haber, L.; Fuh, G. Improving Antibody Binding Affinity and Specificity for Therapeutic Development. In *Therapeutic Antibodies: Methods and Protocols*; Dimitrov, A. S., Ed.; Methods in Molecular Biology™; Humana Press: Totowa, NJ, 2009; pp 353–376. https://doi.org/10.1007/978-1-59745-554-1_19.

(28) Gahmberg, C. G.; Fagerholm, S. C.; Nurmi, S. M.; Chavakis, T.; Marchesan, S.; Grönholm, M. Regulation of Integrin Activity and Signalling. *Biochimica et Biophysica Acta (BBA) - General Subjects* **2009**, *1790* (6), 431–444. https://doi.org/10.1016/j.bbagen.2009.03.007.

(29) Puklin-Faucher, E.; Gao, M.; Schulten, K.; Vogel, V. How the Headpiece Hinge Angle Is Opened: New Insights into the Dynamics of Integrin Activation. *J Cell Biol* **2006**, *175* (2), 349–360. https://doi.org/10.1083/jcb.200602071.

(30) Lee, J.-O.; Rieu, P.; Arnaout, M. A.; Liddington, R. Crystal Structure of the A Domain from the a Subunit of Integrin CR3 (CD11 b/CD18). *Cell* **1995**, *80* (4), 631–638. https://doi.org/10.1016/0092-8674(95)90517-0.

(31) Takagi, J.; Petre, B. M.; Walz, T.; Springer, T. A. Global Conformational Rearrangements in Integrin Extracellular Domains in Outside-In and Inside-Out Signaling. *Cell* **2002**, *110* (5), 599–611. https://doi.org/10.1016/S0092-8674(02)00935-2.

(32) Xiong, J.-P.; Stehle, T.; Zhang, R.; Joachimiak, A.; Frech, M.; Goodman, S. L.; Arnaout, M. A. Crystal Structure of the Extracellular Segment of Integrin AVβ3 in Complex with an Arg-Gly-Asp Ligand. *Science* **2002**, *296* (5565), 151–155. https://doi.org/10.1126/science.1069040.

(33) Mohiuddin, E.; Wakimoto, H. Extracellular Matrix in Glioblastoma: Opportunities for Emerging Therapeutic Approaches. *Am J Cancer Res* **2021**, *11* (8), 3742–3754.

(34) Bachman, H.; Nicosia, J.; Dysart, M.; Barker, T. H. Utilizing Fibronectin Integrin-Binding Specificity to Control Cellular Responses. *Adv Wound Care (New Rochelle)* **2015**, *4* (8), 501–511. https://doi.org/10.1089/wound.2014.0621.

(35) Belkin, A. M.; Stepp, M. A. Integrins as Receptors for Laminins. *Microsc Res Tech* **2000**, *51* (3), 280–301. https://doi.org/10.1002/1097-0029(20001101)51:3<280::AID-JEMT7>3.0.CO;2-O.

(36) Boateng, S. Y.; Lateef, S. S.; Mosley, W.; Hartman, T. J.; Hanley, L.; Russell, B. RGD and YIGSR Synthetic Peptides Facilitate Cellular Adhesion Identical to That of Laminin and Fibronectin but Alter the Physiology of Neonatal Cardiac Myocytes. *American Journal of Physiology-Cell Physiology* **2005**, *288* (1), C30–C38. https://doi.org/10.1152/ajpcell.00199.2004.

(37) Koivunen, E.; Wang, B.; Ruoslahti, E. Isolation of a Highly Specific Ligand for the Alpha 5 Beta 1 Integrin from a Phage Display Library. *J Cell Biol* **1994**, *124* (3), 373–380. https://doi.org/10.1083/jcb.124.3.373.

(38) Danhier, F.; Le Breton, A.; Préat, V. RGD-Based Strategies To Target Alpha(v) Beta(3) Integrin in Cancer Therapy and Diagnosis. *Mol. Pharmaceutics* **2012**, *9* (11), 2961–2973. https://doi.org/10.1021/mp3002733.

(39) Sloan-Dennison, S.; Schultz, Z. D. Label-Free Plasmonic Nanostar Probes to Illuminate in Vitro Membrane Receptor Recognition. *Chem. Sci.* **2019**, *10* (6), 1807–1815. https://doi.org/10.1039/C8SC05035J.

(40) Rist, D.; DePalma, T.; Stagner, E.; Tallman, M. M.; Venere, M.; Skardal, A.; Schultz, Z. D. Cancer Cell Targeting, Magnetic Sorting, and SERS Detection through Cell Surface Receptors. *ACS Sens.* **2023**, *8* (12), 4636–4645. https://doi.org/10.1021/acssensors.3c01625.

(41) Bassan, P.; Byrne, H. J.; Bonnier, F.; Lee, J.; Dumas, P.; Gardner, P. Resonant Mie Scattering in Infrared Spectroscopy of Biological Materials – Understanding the 'Dispersion Artefact.' *Analyst* **2009**, *134* (8), 1586. https://doi.org/10.1039/b904808a.

(42) Stiles, P. L.; Dieringer, J. A.; Shah, N. C.; Van Duyne, R. P. Surface-Enhanced Raman Spectroscopy. *Annual Rev. Anal. Chem.* **2008**, *1* (1), 601–626. https://doi.org/10.1146/annurev.anchem.1.031207.112814.

(43) Zhang, D.; Li, C.; Zhang, C.; Slipchenko, M. N.; Eakins, G.; Cheng, J.-X. Depth-Resolved Mid-Infrared Photothermal Imaging of Living Cells and Organisms with Submicrometer Spatial Resolution. *Science Advances* **2016**, *2* (9), e1600521. https://doi.org/10.1126/sciadv.1600521.

(44) Klementieva, O.; Sandt, C.; Martinsson, I.; Kansiz, M.; Gouras, G. K.; Borondics, F. Super-Resolution Infrared Imaging of Polymorphic Amyloid Aggregates Directly in Neurons. *Advanced Science* **2020**, *7* (6), 1903004. https://doi.org/10.1002/advs.201903004.

(45) Huang, N.; Short, M.; Zhao, J.; Wang, H.; Lui, H.; Korbelik, M.; Zeng, H. Full Range Characterization of the Raman Spectra of Organs in a Murine Model. *Opt. Express, OE* **2011**, *19* (23), 22892–22909. https://doi.org/10.1364/OE.19.022892.

(46) Oh, S. J.; Cook, D. C.; Townsend, H. E. Characterization of Iron Oxides Commonly Formed as Corrosion Products on Steel. *Hyperfine Interactions* **1998**, *112* (1), 59–66. https://doi.org/10.1023/A:1011076308501.

(47) Nawaz, H.; Bonnier, F.; Meade, A. D.; Lyng, F. M.; Byrne, H. J. Comparison of Subcellular Responses for the Evaluation and Prediction of the Chemotherapeutic Response to Cisplatin in Lung Adenocarcinoma Using Raman Spectroscopy. *Analyst* **2011**, *136* (12), 2450–2463. https://doi.org/10.1039/C1AN15104E.

(48) Chan, J. W.; Taylor, D. S.; Zwerdling, T.; Lane, S. M.; Ihara, K.; Huser, T. Micro-Raman Spectroscopy Detects Individual Neoplastic and Normal Hematopoietic Cells. *Biophysical Journal* **2006**, *90* (2), 648–656. https://doi.org/10.1529/biophysj.105.066761.

(49) Krimm, S.; Bandekar, J. Vibrational Spectroscopy and Conformation of Peptides, Polypeptides, and Proteins. In *Advances in Protein Chemistry*; Anfinsen, C. B., Edsall, J. T., Richards, F. M., Eds.; Academic Press, 1986; Vol. 38, pp 181–364. https://doi.org/10.1016/S0065-3233(08)60528-8.

(50) Dong, A.; Huang, P.; Caughey, W. S. Protein Secondary Structures in Water from Second-Derivative Amide I Infrared Spectra. *Biochemistry* **1990**, *29* (13), 3303–3308. https://doi.org/10.1021/bi00465a022.

(51) Inan Genç, A.; Gok, S.; Banerjee, S.; Severcan, F. Valdecoxib Recovers the Lipid Composition, Order and Dynamics in Colon Cancer Cell Lines Independent of COX-2 Expression: An ATR-FTIR Spectroscopy Study. *Appl Spectrosc* **2017**, *71* (1), 105–117. https://doi.org/10.1177/0003702816654164.

(52) Gao, Y.; Huo, X.; Dong, L.; Sun, X.; Sai, H.; Wei, G.; Xu, Y.; Zhang, Y.; Wu, J. Fourier Transform Infrared Microspectroscopy Monitoring of 5-Fluorouracil-Induced Apoptosis in SW620 Colon Cancer Cells. *Molecular Medicine Reports* **2015**, *11* (4), 2585–2591. https://doi.org/10.3892/mmr.2014.3088.

(53) Kneipp, J.; Lasch, P.; Baldauf, E.; Beekes, M.; Naumann, D. Detection of Pathological Molecular Alterations in Scrapie-Infected Hamster Brain by Fourier Transform Infrared (FT-IR) Spectroscopy. *Biochimica et Biophysica Acta (BBA) - Molecular Basis of Disease* **2000**, *1501* (2), 189–199. https://doi.org/10.1016/S0925-4439(00)00021-1.

(54) Akkas, S. B.; Severcan, M.; Yilmaz, O.; Severcan, F. Effects of Lipoic Acid Supplementation on Rat Brain Tissue: An FTIR Spectroscopic and Neural Network Study. *Food Chemistry* **2007**, *105* (3), 1281–1288. https://doi.org/10.1016/j.foodchem.2007.03.015.

(55) Ozek, N. S.; Tuna, S.; Erson-Bensan, A. E.; Severcan, F. Characterization of MicroRNA-125b Expression in MCF7 Breast Cancer Cells by ATR-FTIR Spectroscopy. *Analyst* **2010**, *135* (12), 3094–3102. https://doi.org/10.1039/C0AN00543F.

(56) Shie, M.; Kharitonenkov, I. G.; Tikhonenko, T. I.; Chirgadze, Y. N. New Possibilities of Investigating Nucleic Acids and Nucleoproteins in Aqueous Solutions by Infrared Spectroscopy. *Nature* **1972**, *235* (5338), 386–388. https://doi.org/10.1038/235386a0.

(57) Adam, S.; Liquier, J.; Taboury, J. A.; Taillandier, E. Right- and Left-Handed Helixes of Poly[d(A-T)].Cntdot.Poly[d(A-T)] Investigated by Infrared Spectroscopy. *Biochemistry* **1986**, *25* (11), 3220–3225. https://doi.org/10.1021/bi00359a021.

(58) Susi, H.; Ard, J. S. Vibrational Spectra of Nucleic Acid Constituents—I: Planar Vibrations of Uracil. *Spectrochimica Acta Part A: Molecular Spectroscopy* **1971**, *27* (9), 1549–1562. https://doi.org/10.1016/0584-8539(71)80211-8.

(59) Benedetti, E.; Bramanti, E.; Papineschi, F.; Rossi, I.; Benedetti, E. Determination of the Relative Amount of Nucleic Acids and Proteins in Leukemic and Normal Lymphocytes by Means of Fourier Transform Infrared Microspectroscopy. *Appl. Spectrosc., AS* **1997**, *51* (6), 792–797.

(60) Lu, K. C.; Prohofsky, E. W.; Van Zandt, L. L. Vibrational Modes of A-DNA, B-DNA, and A-RNA Backbones: An Application of a Green-Function Refinement Procedure. *Biopolymers* **1977**, *16* (11), 2491–2506. https://doi.org/10.1002/bip.1977.360161112.

(61) Dalton, S. L.; Scharf, E.; Briesewitz, R.; Marcantonio, E. E.; Assoian, R. K. Cell Adhesion to Extracellular Matrix Regulates the Life Cycle of Integrins. *MBoC* **1995**, *6* (12), 1781–1791. https://doi.org/10.1091/mbc.6.12.1781.

(62) Danen, E. H. J.; Yamada, K. M. Fibronectin, Integrins, and Growth Control. *Journal of Cellular Physiology* **2001**, *189* (1), 1–13. https://doi.org/10.1002/jcp.1137.

(63) Schwartz, M. A.; Assoian, R. K. Integrins and Cell Proliferation: Regulation of Cyclin-Dependent Kinases via Cytoplasmic Signaling Pathways. *Journal of Cell Science* **2001**, *114* (14), 2553–2560. https://doi.org/10.1242/jcs.114.14.2553.

(64) Shroff, K.; Pearce, T. R.; Kokkoli, E. Enhanced Integrin Mediated Signaling and Cell Cycle Progression on Fibronectin Mimetic Peptide Amphiphile Monolayers. *Langmuir* **2012**, *28* (3), 1858–1865. https://doi.org/10.1021/la203322t.

(65) Salem, C.; El-Alfy, M.; Leblond, C. P. Changes in the rate of RNA synthesis during the cell cycle. *The Anatomical Record* **1998**, *250* (1), 6–12. https://doi.org/10.1002/(SICI)1097-0185(199801)250:1<6::AID-AR2>3.0.CO;2-4.

(66) Boydston-White, S.; Gopen, T.; Houser, S.; Bargonetti, J.; Diem, M. Infrared Spectroscopy of Human Tissue. V. Infrared Spectroscopic Studies of Myeloid Leukemia (ML-1) Cells at Different Phases of the Cell Cycle. *Biospectroscopy* **1999**, *5* (4), 219–227. https://doi.org/10.1002/(SICI)1520-6343(1999)5:4<219::AID-BSPY2>3.0.CO;2-O.

(67) R. Whelan, D.; R. Bambery, K.; Puskar, L.; McNaughton, D.; R. Wood, B. Synchrotron Fourier Transform Infrared (FTIR) Analysis of Single Living Cells Progressing through the Cell Cycle. *Analyst* **2013**, *138* (14), 3891–3899. https://doi.org/10.1039/C3AN00316G.

(68) Hu, J.; Song, J.; Tang, Z.; Wei, S.; Chen, L.; Zhou, R. Hypericin-Mediated Photodynamic Therapy Inhibits Growth of Colorectal Cancer Cells via Inducing S Phase Cell Cycle Arrest and Apoptosis. *European Journal of Pharmacology* **2021**, *900*, 174071. https://doi.org/10.1016/j.ejphar.2021.174071.

(69) Liu, J.; Li, Q.; Liu, Z.; Lin, L.; Zhang, X.; Cao, M.; Jiang, J. Harmine Induces Cell Cycle Arrest and Mitochondrial Pathway-Mediated Cellular Apoptosis in SW620 Cells via Inhibition of the Akt and ERK Signaling Pathways. *Oncology Reports* **2016**, *35* (6), 3363–3370. https://doi.org/10.3892/or.2016.4695.

TOC Artwork